Optimized Integrated Harmonic Filter Inductor for Dual-Converter-Fed Open-End Transformer Topology

Gohil, Ghanshyamsinh Vijaysinh; Bede, Lorand; Teodorescu, Remus; Kerekes, Tamas; Blaabjerg, Frede

Published in:
I E E E Transactions on Power Electronics

DOI (link to publication from Publisher):
10.1109/TPEL.2016.2562679

Publication date:
2017

Document Version
Early version, also known as pre-print

Optimized Integrated Harmonic Filter Inductor for Dual-Converter Fed Open-End Transformer Topology

Ghanshyamsinh Gohil, *Student Member, IEEE,* Lorand Bede, *Student Member, IEEE,*
Remus Teodorescu, *Fellow, IEEE,* Tamas Kerekes, *Senior Member, IEEE,* and Frede Blaabjerg, *Fellow, IEEE*

***Abstract*—Many high power converter systems are often connected to the medium voltage network using a step-up transformer. In such systems, the converter-side windings of the transformer can be configured as an open-end and multi-level voltage waveforms can be achieved by feeding these open-end windings from both ends using the two-level dual-converter. An LCL filter with separate converter-side inductors for each of the converter is commonly used to attenuate the undesirable harmonic frequency components in the grid current. The magnetic integration of the converter-side inductors is presented in this paper, where the flux in the common part of the magnetic core is completely canceled out. As a result, the size of the magnetic component can be significantly reduced. A multi-objective design optimization is presented, where the energy loss and the volume are optimized. The optimization process takes into account the yearly load profile and the energy loss is minimized, rather than minimizing the losses at a specific operating point. The size reduction achieved by the proposed inductor is demonstrated through a comparative evaluation. Finally, the analysis is supported through simulations and experimental results.**

***Index Terms*—Voltage source converters (VSC), dual-converter, filter design, open-end transformer topology, multi-objective optimization, integrated inductor, harmonic filter, magnetic integration**

I. Introduction

Many high power converter systems are often connected to the medium voltage network and a step-up transformer is used to match the voltage levels of the converter with the medium voltage grid. In some applications, the transformer is also required for providing galvanic isolation. In such systems, the converter-side windings of the transformer can be configured as an open-end. This open-end transformer winding can be fed from both the ends using the two-level Voltage Source Converters (VSCs) [1], as shown in Fig. 1. The number of levels in the output voltages is the same as that of the three level Neutral point clamped (NPC) converter and each of the two-level VSC operates with the half of the dc-link voltage than the dc-link voltage required for the three level NPC. This enables simple and proven two-level VSC to be used in medium voltage applications. For example, 3.3 kV converter system can be realized using the dual-converter with two-level VSCs having a switch voltage rating of 4.5 kV. However, Common Mode (CM) circulating current flows through the closed path if both the VSCs are connected to a common dc-link. The CM circulating current can be suppressed either by using the CM choke [2], [3] or by employing a proper Pulse Width Modulation (PWM) scheme to ensure complete elimination of the CM voltage [4], [5]. However, in many applications, isolated dc-links can be derived from the source itself and such extra measures for CM circulating current suppression may not be required. For example, the isolated dc-links can be obtained in

1) PhotoVoltaic (PV) systems by dividing the total number of arrays into two groups to form separate dc-links [1].
2) Wind Energy Conversion System (WECS): isolated dc-links can be obtained by using a dual stator-winding generator [6].

Therefore the analysis presented in this paper is mainly focused on the dual converter fed open-end transformer topology with two separate dc-links.

For the grid-connected applications, utilities impose stringent harmonic current injection limits. In order to obey this limits, high-order harmonic filter is often employed. An LCL harmonic filter is commonly used in high power grid-connected applications [7] and one of the possible arrangement of the LCL filter for the dual-converter fed open-end transformer topology is shown in Fig. 1. The leakage inductance of the transformer is considered to be a part of the grid-side inductor of the LCL filter. Two VSCs (denoted as High-Side Converter (HSC) and Low-Side Converter (LSC) in Fig. 1) are connected to a common shunt capacitive branch of the LCL filter through the converter-side inductors L_{f_H} and L_{f_L},

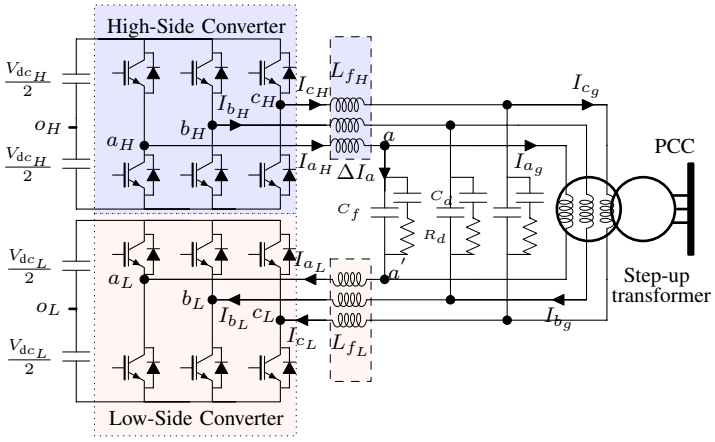

Fig. 1. The system configuration of the dual converter fed open-end winding transformer topology with two separate dc-links. The open-end primary windings are fed from two-level voltage source converters.

respectively. The magnetic integration of the L_{f_H} and L_{f_L} is presented in this paper. As a result of this magnetic integration, the flux in the common part of the magnetic core is completely canceled out. This leads to substantial reduction in the size of the converter-side inductor.

The detailed design procedure for the proposed integrated inductor is also presented in this paper. For proper design, It is important to investigate the design trade-offs and choose an optimum solution. The optimization can be performed with an objective to minimize losses, volume or cost. An analytical optimization to minimize winding losses is presented in [8]–[10]. The procedure to optimize the inductor volume is presented in [11]. However, the volume optimized design may have higher losses. Therefore it is important to investigate the tradeoff between losses and volume, which can be achieved by performing multi-objective optimization. The multi-objective optimization of the LC output filter is presented in [12], where the optimization is carried out for a specific loading condition. However the obtained solution may not be optimal when the load varies in a large range. Therefore, the mission profile based multi-objective optimization approach for the proposed integrated inductor has been adopted in this paper.

This paper is organized as follows: The operation principle of the dual-converter fed open-end transformer topology is briefly discussed in Section II. The magnetic structure of the proposed integrated inductor is described in Section III. Section IV discusses the design procedure in general and the multi-objective optimization of the integrated inductor. The size reduction achieved by the magnetic integration is also demonstrated by comparing the volume of the integrated inductor with the separate inductor case for the 6.6 MVA, 3.3 kV WECS and it is presented in Section V. The simulation and the experimental results are finally presented in Section VI.

II. Dual-Converter Fed Open-End Transformer Topology

The operation of the dual-converter fed open-end transformer converter is briefly described in this section. The dual-converter system consists of the HSC and the LSC is shown in Fig. 1. A Two-level VSC is used for both the HSC and the LSC.

The reference voltage space vector $\overrightarrow{V^*}$ is synthesized by modulating the HSC and the LSC. The magnitude of the reference voltage space vectors of the HSC and the LSC is half than that of the desired reference voltage space vector $\overrightarrow{V^*}$ ($|\overrightarrow{V_H^*}| = |\overrightarrow{V_L^*}| = |\overrightarrow{V^*}|/2$). The reference voltage space vector angle of the HSC is the same as that of the desired voltage space vector ($\psi_H = \psi$), whereas the reference voltage space vector angle of the LSC is shifted by an angle $180°$ ($\psi_L = \psi_H + 180°$), as shown in Fig. 2.

From Fig. 1, the voltage across the shunt capacitive branch C_f of the LCL filter is given as

$$V_{xx'} = (V_{x_H o_H} - V_{x_L o_L}) - L_{f_H}\frac{dI_{x_H}}{dt} - L_{f_L}\frac{dI_{x_L}}{dt} + V_{o_H o_L} \quad (1)$$

where the subscript x represents the phases $x = \{a, b, c\}$. As the dc-links are separated, the common-mode components of the voltages in (1) do not drive any common-mode circulating current. As a result, only the differential mode current would flow through the inductors. From Fig. 1, the converter-side current of the HSC can be obtained as

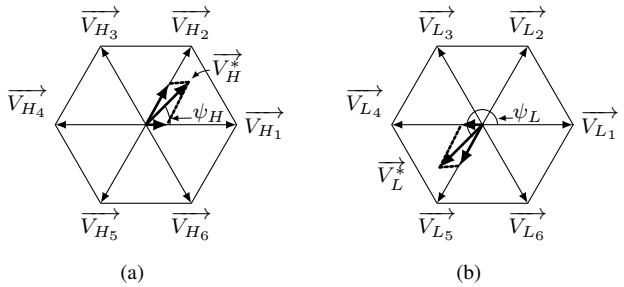

Fig. 2. Reference voltage space vector and its formation by the geometrical summation. (a) Reference voltage space vector for the HSC, (b) Reference voltage space vector for the LSC.

$$I_{x_H} = I_{x_g} + \Delta I_x \quad (2)$$

where I_{x_g} is the current through the low-voltage side of the transformer winding and ΔI_x is the current through the shunt branch of the LCL filter. Similarly, the converter-side current of the LSC is given as

$$I_{x_L} = I_{x_g} + \Delta I_x \quad (3)$$

From (2) and (3), it is evident that the converter-side currents of the HSC and the LSC are equal:

$$I_{x_H} = I_{x_L} = I_x \quad (4)$$

where I_{x_H} and I_{x_L} are the phase x currents of the HSC and LSC, respectively. Assuming $L_{f_H} = L_{f_L} = L_f/2$ and using (1) and (4), the voltage across the converter-side inductor is given as

$$L_f\frac{dI_x}{dt} = V_{x_H x} + V_{x'x_L} = (V_{x_H o_H} - V_{x_L o_L}) - V_{xx'} + V_{o_H o_L} \quad (5)$$

where L_f is the equivalent converter-side inductance of the LCL filter. A single magnetic component with the inductance L_f is realized by the magnetic integration of the L_{f_H} and L_{f_L} and the structure is discussed in the following section.

III. Integrated Inductor

The size and weight of the magnetic components can be reduced through magnetic integration [13]–[17]. For a three-phase three-wire systems, the sum of the phase currents is always zero. This property is exploited in three-phase magnetic structure, where three single-phase magnetic components are combined to achieve smaller three-phase single magnetic structure. The principle of magnetic integration in a power electronic circuit was introduced for the DC-DC converters in [18], where two inductors are magnetically integrated into single magnetic component without compromising the functionality, while significantly reducing the size, weight, and losses. The integration of the converter-side inductor and the grid-side inductor of the harmonic LCL filter is proposed in [19] and the volume reduction is demonstrated. In many grid-connected applications, transformers are used to match the

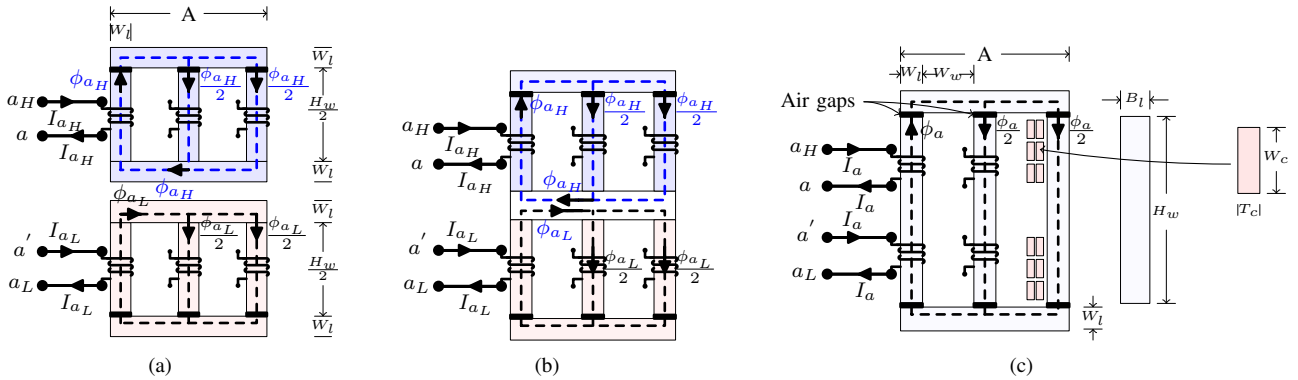

Fig. 3. Magnetic structure. (a) Separate inductors for the HSC and the LSC, (b) Flux cancellation through magnetic integration, (c) Proposed integrated inductor.

converter voltage level with the grid voltage level. In such systems, the functionalities of the harmonic filter inductors and the transformer can be integrated into single magnetic component [20].

The magnetic integration of the converter-side inductors of the HSC and LSC of the dual-converter fed open-end transformer topology is presented in this paper. A three-phase inductor is chosen for the illustration due its wide-spread use in the high power applications. However, it is important to point out that the same analysis can be used for the single-phase inductor as well.

The magnetic structure of the three-phase three-limb converter-side inductor for both the HSC and the LSC are shown in Fig. 3(a). These two inductors can be magnetically integrated as shown in Fig. 3(b), where both the inductors share a common magnetic path. The magnetic structure has six limbs, on which the coils are wound. The upper three limbs belong to the L_{f_H}, whereas the lower three limbs receive the coils corresponding to the L_{f_L}. The upper limbs are magnetically coupled using the top bridge yoke, whereas the lower three limbs are magnetically coupled using the bottom bridge yoke. The upper and the lower limbs share a common yoke, as shown in Fig. 3(b).

Considering three-phase three-wire system

$$I_a + I_b + I_c = 0 \tag{6}$$

and at a particular instance

$$I_a = -(I_b + I_c) \tag{7}$$

The flux distribution in the magnetic structure for this case (the positive value of the I_a and the negative values of the I_b and I_c) is shown in Fig. 3(b).

The simplified reluctance model of this magnetic structure is shown in Fig. 4, where $\Re_L$, $\Re_g$, and $\Re_Y$ are the reluctances of the limb, the air gap, the top and the bottom bridge yokes, respectively. The leakage flux path is represented by the reluctance $\Re_\sigma$. The reluctance of the common yoke is represented as $\Re_{Y1}$. ϕ_{a_H}, ϕ_{b_H}, and ϕ_{c_H} are the fluxes in the upper three limbs whereas ϕ_{a_L}, ϕ_{b_L}, and ϕ_{c_L} are the fluxes in the lower three limbs. ϕ_1, and ϕ_2 represent the fluxes in the common yokes, as shown in Fig. 4. By exploiting the unique property of open-end transformer topology, in which

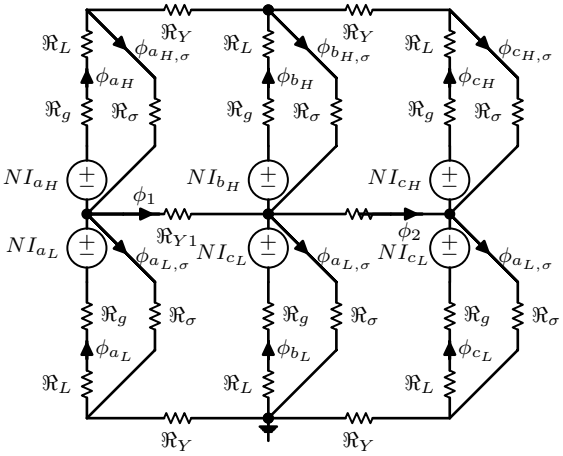

Fig. 4. Simplified reluctance model of the magnetic structure shown in Fig. 3(b).

the converter-side current of a particular phase of the HSC and LSC is always equal ($I_{x_H} = I_{x_L} = I_x$) and By solving the reluctance network, the fluxes in the common yokes are obtained as

$$\phi_1 = 0,\ \phi_2 = 0 \tag{8}$$

The flux components in the common yoke (ϕ_1 and ϕ_2) are zero and therefore the common yoke can be completely removed, as shown in Fig. 3(c). The integrated inductor has only two yokes, compared to four in the case of the separate inductors. As a result, substantial reduction in the volume of the inductor can be achieved through magnetic integration of L_{f_H} and L_{f_L}.

For the integrated inductor, the induced voltage across the coil a_H is given as

$$\begin{aligned} V_{a_H a} = {} & L_{a_H a_H}\frac{dI_{a_H}}{dt} - L_{a_H b_H}\frac{dI_{b_H}}{dt} - L_{a_H c_H}\frac{dI_{c_H}}{dt} \\ & + L_{a_H a_L}\frac{dI_{a_L}}{dt} - L_{a_H b_L}\frac{dI_{b_L}}{dt} - L_{a_H c_L}\frac{dI_{c_L}}{dt} \end{aligned} \tag{9}$$

For the magnetic structure shown in Fig. 3(c), the reluctance of the central limb is $2(\Re_g + \Re_L)$, whereas the reluctance of the side-limbs is $2(\Re_g + \Re_L + \Re_Y)$. This introduces some asymmetry in three-phase system. However, the reluctance of the air gap $\Re_g$ is very large compared to the reluctance of

the magnetic path (both $\Re_L$ and $\Re_Y$). Moreover, the length of the yoke is also small compared to the length of the limbs for the commercially available cores [21]. For the magnetic structure shown in Fig. 3(c), $\Re_L/\Re_Y$ is typically in the range of 5-7. As a result, $\Re_Y$ can be neglected and the magnetic structure can be assumed symmetrical. With this assumption, the self-inductance of each of the coils is obtained as

$$L_s = N^2\Big[\frac{1}{\Re_\sigma(1+\frac{\Re_L}{\Re_\sigma}+\frac{\Re_g}{\Re_\sigma})}+\frac{1}{3\Re_g(1+\frac{\Re_L}{\Re_\sigma}+\frac{\Re_g}{\Re_\sigma})(1+\frac{\Re_L}{\Re_g})}\Big] \tag{10}$$

The mutual inductance between the two coils of the same phase can be obtained as

$$L_{x_H x_L} = k_{x_H x_L} L_s = L_s\Big[\frac{1+\frac{\Re_L}{\Re_\sigma}+\frac{\Re_g}{\Re_\sigma}}{1+3\frac{\Re_L}{\Re_\sigma}+3\frac{\Re_g}{\Re_\sigma}}\Big] \tag{11}$$

where $k_{x_H x_L}$ is the coupling coefficient between the coils that belong to the same phase. The mutual inductance between the two coils of the different phases are given as

$$\begin{aligned} M &= L_{a_H b_H} = L_{b_H c_H} = L_{c_H a_H} \\ &= \frac{1}{2}L_s\Big[\frac{1+\frac{\Re_L}{\Re_\sigma}+\frac{\Re_g}{\Re_\sigma}}{1+3\frac{\Re_L}{\Re_\sigma}+3\frac{\Re_g}{\Re_\sigma}}\Big]\Big[\frac{1}{1+\frac{\Re_L}{\Re_\sigma}+\frac{\Re_g}{\Re_\sigma}}\Big] \end{aligned} \tag{12}$$

Substituting the inductance values in (9) yields

$$V_{a_H a} = L_s(1+k_{x_H x_L})\frac{dI_a}{dt} - 2M(\frac{dI_b}{dt}+\frac{dI_c}{dt}) \tag{13}$$

Using (6) and (13), the induced voltage across the coil a_H is given as

$$V_{a_H a} = [L_s(1+k_{x_H x_L})+2M]\frac{dI_a}{dt} \tag{14}$$

Similarly, the induced voltage across the coil a_L is given as

$$V_{a' a_L} = [L_s(1+k_{x_H x_L})+2M]\frac{dI_a}{dt} \tag{15}$$

Using (5), (14), and (15), the equivalent inductance is obtained as

$$L_f = 2[L_s(1+k_{x_H x_L})+2M] \tag{16}$$

Assuming $\Re_\sigma >> \Re_L$, $\Re_\sigma >> \Re_g$, and $\Re_g >> \Re_L$, the simplified expression for the L_f is obtained as

$$L_f \approx \frac{2N^2}{\Re_g} \approx \frac{2\mu_0 N^2 A_g^{'}}{l_g} \tag{17}$$

where μ_0 is the permeability of the free space, l_g is the length of the air gap of one limb and $A_g^{'}$ is the effective cross-sectional area of the air gap after considering the effects of the fringing flux. The effective cross-sectional area of the air gap $A_{g'}$ is obtained by evaluating the cross-section area of the air gap after adding l_g to each dimension in the cross-section.

IV. Design of the Integrated Inductor

A design methodology is demonstrated in this section by carrying out the design of the integrated inductor for the high power WECS. The system specifications of the WECS is given in Table I. The WECS operates with the power factor close to unity. In this case, the 60° Discontinuous Pulse-Width Modulation (commonly referred to as a DPWM1 [22]) scheme could result up to 50% switching loss reduction compared to the continuous modulation scheme. Therefore DPWM1 is used to modulate the HSC and the LSC. Using this specifications, design of the integrated inductor is carried out and the design steps are illustrated hereafter.

TABLE I
System specifications and parameters for simulation and hardware study

Parameters	Simulations	Experiment
Power S	6.6 MVA (6 MW)	11 kVA (10 kW)
Switching frequency f_{sw}	900 Hz	900 Hz
AC voltage (line-to-line) V_{ll}	3300 V	400 V
Rated current	1154 A	15.8 A
DC-link voltage ($V_{\mathrm{dc}_H} = V_{\mathrm{dc}_L}$)	2800 V	330 V
Modulation index range	$0.95 \leq \mathrm{M} \leq 1.15$	$0.95 \leq \mathrm{M} \leq 1.15$
L_g (including transformer leakage)	525 μH (0.1 pu)	4.2 mH (0.1 pu)

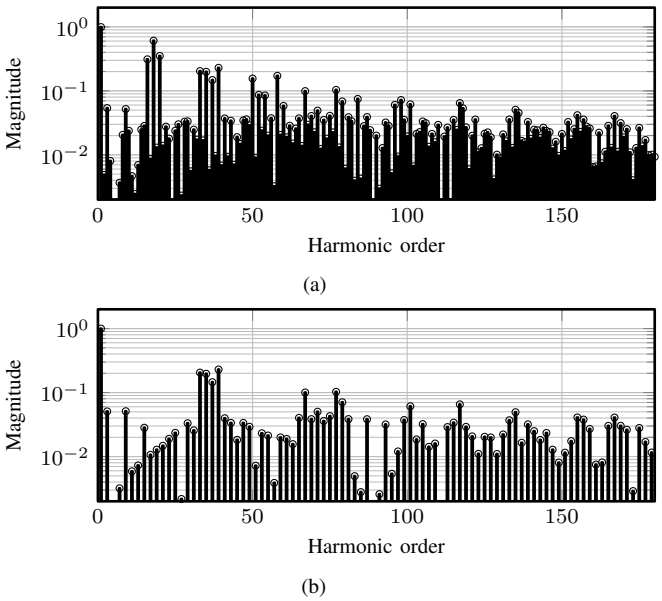

Fig. 5. Simulated harmonic spectrum of the switched voltages with the modulation index $M = 1$ and the switching frequency of 900 Hz. (a) Switched output voltage of the high-side converter $V_{a_H o_H}$ (normalized with respect to the $V_{\mathrm{dc}}/2$), (b) Resultant voltage ($V_{a_H o_H} - V_{a_L o_L}$) (normalized with respect to the V_{dc}).

A. Value of the converter-side inductor L_f

The harmonic spectra of the switched output voltage of the HSC is shown in Fig. 5(a). The major harmonic components in the switched output voltage of the individual converter appears at the carrier frequency (900 Hz), whereas these components are substantially reduced in the resultant voltage, as shown in Fig. 5(b). The spectrum comprises the maximum values of the individual voltage harmonic components of the resultant voltage, over the entire operating range is obtained and it is defined as a Virtual Voltage Harmonic Spectrum (VVHS) [23]. The LCL harmonic filter is designed such that the enough impedance is offered to the harmonic frequency components so that the individual harmonic components of the injected grid-currents remain within the specified limits.

The harmonic current injection limit for a generator con-

TABLE II
BDEW HARMONIC CURRENT INJECTION LIMITS FOR THE WECS CONNECTED TO THE 10 KV MEDIUM VOLTAGE NETWORK

Harmonic Order h	Current Injection Limit (A/MVA/SCR)
5	0.019
7	0.027
11	0.017
13	0.013
17	0.007
19	0.006
23	0.004
25	0.003
odd-ordered $25 < h < 40$	0.075 / h
Even-ordered $h < 40$	0.02 / h
$40 < h < 180$	0.06 / h

nected to the medium-voltage network, specified by the German Association of Energy and Water Industries (BDEW) [23]–[25], is considered in this paper. The permissible harmonic current injection is determined by the apparent power of the WECS and the Short-Circuit Ratio (SCR) at the Point of the Common Coupling (PCC). The maximum current injection limit of the individual harmonic components up to 9 kHz is specified in the standard and the limits for the WECS connected to the 30 KV medium-voltage network are given in Table II. Special limits are set for the odd-ordered integer harmonics below the 25th harmonic, as given in Table II. The SCR is taken to be 20 and the allowable injection limits of individual harmonic components on the low voltage side (3300 V) for the 6.6 MVA WECS are calculated.

Using VVHS and the specified values of the permissible harmonic injection, the required admittance for the hth harmonic component is obtained as

$$Y_h^* = \frac{I_{h,BDEW}^*}{V_{h,VVHS}} \tag{18}$$

where $I_{h,BDEW}^*$ is the specified BDEW current injection limit of the hth harmonic component (refer to [24]) and $V_{h,VVHS}$ is the maximum values of the hth harmonic components over the entire operating range. The value of the filter parameters are then chosen such that the designed filter has a lower admittance than the required value of the filter admittance for all the harmonic frequency components of interest (upto 180th harmonic frequency component in case of the BDEW standard) [26], [27].

For the LCL filter, the filter admittance is given as

$$Y_{LCL}(s) = \frac{I_g(s)}{V_{PWM}(s)}\bigg|_{V_g=0} = \frac{1}{L_f L_g C_f}\frac{1}{s(s^2+\omega_{r,LCL}^2)} \tag{19}$$

Using this expression the filter admittance for individual harmonic frequency component is evaluated and the values of the LCL filter components are obtained. Once the value of L_f is obtained, an optimized design can be carried out.

B. Core Loss Modeling

The Improved Generalized Steinmetz Equation (IGSE) [28], [29] is used to calculate the core losses. The core losses per unit volume is given as

$$P_{fe,v} = \frac{1}{T}\int_0^T k_i \left|\frac{dB(t)}{dt}\right|^{\alpha}(\Delta B)^{\beta-\alpha}dt \tag{20}$$

where α, β and k_i are the constants determined by the material characteristics. ΔB is the peak-to-peak value of the flux density and T is the switching interval. The flux waveform has major and minor loops and these loops are evaluated separately.

1) Major Loop: Assuming the inductance value to be constant, the flux density in the limb is given as

$$B_x(t) = \frac{L_f I_{x,f}(t)}{2NA_c} \tag{21}$$

where A_c is the cross-sectional area of the limb, $I_{x,f}$ is the fundamental component of the current.

2) Minor Loop: The reference space vector $\overrightarrow{V_H^*}$ and $\overrightarrow{V_L^*}$ are synthesized using active and zero voltage vectors and the volt-second balance is maintained by choosing appropriate dwell time of these vectors. The application of the discrete vectors results in an error between the applied voltage vector and the reference voltage vector, as shown in Fig. 6 for the HSC. The error voltage vector during the kth state in a switching cycle is given as

$$\overrightarrow{\boldsymbol{V}}_{\boldsymbol{H,err,k}} = \overrightarrow{\boldsymbol{V_k}} - \overrightarrow{\boldsymbol{V_H}} \tag{22}$$

where $\overrightarrow{\boldsymbol{V_H}}$ is the reference space vector and $\overrightarrow{\boldsymbol{V_k}}$ is the VSC voltage vector during kth state. When the space voltage vector is in sector I ($0° \le \psi \le 60°$), $\overrightarrow{\boldsymbol{V_k}} = \{\overrightarrow{\boldsymbol{V_1}}, \overrightarrow{\boldsymbol{V_2}}, \overrightarrow{\boldsymbol{V_z}}\}$. Similarly, the error voltage vectors for the LSC also exists due to the finite sampling. These error voltage vectors lead to the minor loop in the flux density waveform and it is evaluated by performing time integral of the error voltage vector.

The time integral of the error voltage vector is known as the harmonic flux vector [30], [31] and the difference of the harmonic flux vectors of the HSC and the LSC are directly proportional to the flux in the integrated inductor. In the reference frame, rotating synchronously at the fundamental frequency, the instantaneous error voltage vectors can be decomposed into d-axis and the q-axis components as (see

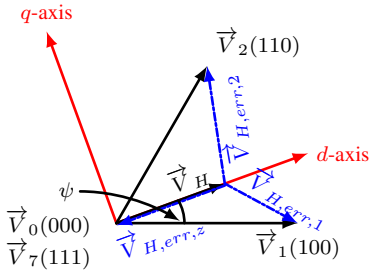

Fig. 6. The active and zero vectors to synthesize given reference vector and corresponding error voltage vectors.

Fig. 6)

$$\begin{aligned}\overrightarrow{\boldsymbol{V}}_{\boldsymbol{H,err,1}} &= \frac{2}{3}V_{dc}\{(\cos\psi_H - \frac{3}{4}M) - j\sin\psi_H\}\\ \overrightarrow{\boldsymbol{V}}_{\boldsymbol{H,err,2}} &= \frac{2}{3}V_{dc}\{[\cos(60^\circ - \psi_H) - \frac{3}{4}M]\\ &\quad + j\sin(60^\circ - \psi_H)\}\\ \overrightarrow{\boldsymbol{V}}_{\boldsymbol{H,err,z}} &= -\frac{1}{2}V_{dc}M\end{aligned} \tag{23}$$

Similarly, the d-axis and the q-axis components of instantaneous error voltage vectors of the LSC are also obtained. Then the difference of the d-axis components of the harmonic flux vectors of the HSC and LSC and the difference of the q-axis components of the harmonic flux vectors of the HSC and LSC are evaluated separately as

$$\begin{aligned}B_{\text{ac},d}(t) &= \frac{1}{2NA_c}\int(\overrightarrow{\boldsymbol{V}}_{\boldsymbol{H,err,d}} - \overrightarrow{\boldsymbol{V}}_{\boldsymbol{L,err,d}})dt\\ B_{\text{ac},q}(t) &= \frac{1}{2NA_c}\int(\overrightarrow{\boldsymbol{V}}_{\boldsymbol{H,err,q}} - \overrightarrow{\boldsymbol{V}}_{\boldsymbol{L,err,q}})dt\end{aligned} \tag{24}$$

Using the d-axis and the q-axis components, the ripple component of the flux density in the limb corresponding to the phase a is obtained as

$$B_a = B_{\text{ac},d}\cos\psi - B_{\text{ac},q}\sin\psi \tag{25}$$

The VSCs are assumed to be modulated using the asymmetrical regularly sampled PulseWidth Modulation (PWM), where the reference voltage space voltage vector is sampled twice in a carrier cycle.

Using this information, the core loss calculations have been carried out for the major loop and each of the minor loops using (20). Then, the total core losses are obtained as

$$P_{fe} = P_{fe,v}V_{fe} \tag{26}$$

where V_{fe} is the volume of the magnetic core.

C. Copper Loss Modeling

The copper loss is evaluated by considering the ac resistance of the winding, which takes into account the skin and proximity effects [32]. The total winding losses of all six coils are [33]

$$P_{cu} = 6R_{dc}\sum_{h=1}^{\infty}k_{p_h}I_{x_h}^2 \tag{27}$$

where

$$\begin{aligned}k_{p_h} =& \sqrt{h}\Delta\Big[\frac{\sinh(2\sqrt{h}\Delta)+\sin(2\sqrt{h}\Delta)}{\cosh(2\sqrt{h}\Delta)-\cos(2\sqrt{h}\Delta)}\\ &+\frac{2}{3}(m^2-1)\frac{\sinh(\sqrt{h}\Delta)-\sin(\sqrt{h}\Delta)}{\cosh(\sqrt{h}\Delta)+\cos(\sqrt{h}\Delta)}\Big]\end{aligned} \tag{28}$$

and $\Delta = T_c/\delta$ and R_{dc} and R_{ac} are the dc and the ac resistance of the coil, respectively. m is the number of layers in the coil, T_c is the thickness of the conductor, and δ is the skin depth. I_{x_h} is the hth harmonic frequency component of the line current I_x. The harmonic spectrum of the resultant voltage is obtained analytically [14] and the hth harmonic frequency component of the line current I_x is obtained as

$$I_{x_h} = Y_{H,LCL}V_h \tag{29}$$

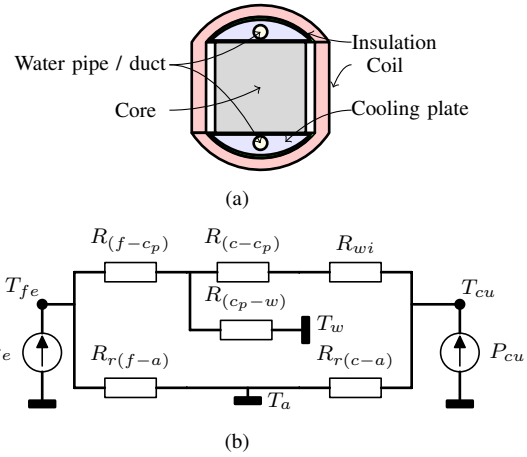

Fig. 7. Simplified thermal model of the integrated inductor. P_{fe} and P_{cu} are the core and copper losses, respectively.

where V_h is the hth harmonic frequency component of the resultant phase voltage and $Y_{H,LCL}$ is the admittance offered by the LCL filter to the hth harmonic frequency component.

D. Thermal Modeling

The liquid cooling for the inductor is considered and the cooling arrangement is shown in Fig. 7(a). The semi-circular aluminum cooling plates with the duct to carry the coolant is considered. This cooling plate is electrically insulated using the epoxy resin. As the heat transfer is anisotropic for the laminated steel, two cooling plates along the edges that are perpendicular to the lamination direction are considered. The hot spot temperature in both the core and the coil (T_{fe} and T_{cu}, respectively) is estimated using the equivalent thermal resistance network [34], shown in Fig. 7(b). For the simplicity of the analysis, the temperature in the core and the coil is assumed to be homogeneous.

The heat transfer mechanism due to the convection and the radiation is considered, where $R_{cv(f-w)}$ and $R_{cv(c-w)}$ are the convection thermal resistance between the core and coolant (water) and between the coil and coolant, respectively. Similarly, $R_{r(f-a)}$ and $R_{r(c-a)}$ represent the radiation thermal resistance between the core and the ambient and between the coil and the ambient, respectively. The radiation thermal resistance value is obtained using the formulas presented in [34].

The thermal resistance between the cooling plate and the coolant is given as

$$R_{(c_p-w)} = \frac{1}{h_{c_p-w}A_{c_p-w}} \tag{30}$$

where h_{c_p-w} is the heat transfer coefficient and A_{c_p-w} is the coolant contact surface. The heat transfer coefficient is

$$h_{c_p-w} = 3130\left(\frac{q}{785.4D_d^2}\right)^{0.87}(100D_d)^{-0.13} \tag{31}$$

where q is the coolant flow rate in [l/s] and D_d is the diameter of the duct in [m]. The thermal resistance between the core and duct surface is given as

$$R_{(f-c_p)} = \frac{2L_{eq}}{\lambda_{cp}(A_{c_pf}+\pi D_d L_d)} + \frac{T_i}{\lambda_i A_{c_pf}} \tag{32}$$

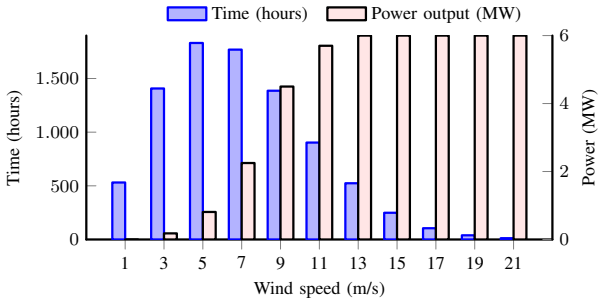

Fig. 8. Wind profile and associated output power of a typical 6 MW wind turbine.

where L_{eq} is the equivalent distance from the cooling surface to the duct, $A_{c_{pf}}$ is the contact area of the cooling plate with the core, L_d is the length of the duct, and λ_{cp} is the thermal conductivity of the aluminum. T_i is the thickness of the insulation and λ_i is the thermal conductivity of the insulation. Using (30) and (32), the thermal resistance between the core and the coolant is obtained as

$$R_{cv(f-w)} = R_{(f-c_p)} + R_{(c_p-w)} \tag{33}$$

In a similar manner, the thermal resistance between the coil and the coolant $R_{cv(c-w)}$ can be also obtained. However, in the heat flow path of the copper losses, there is an additional layer of the insulation material, which is represented as R_{wi} in Fig.7(b).

E. Loading Profile and Energy Yield

The typical wind profile and the power output of a wind turbine over an one year span is shown in Fig. 8. As it is evident from Fig. 8, the power processes by the converter varies in large range and optimizing the inductor for a specific loading condition may result in the suboptimal overall performance. Therefore, instead of optimizing the inductor efficiency at specific loading condition, the energy loss is minimized. In addition to the energy loss minimization, the volume minimization is also considered and multi-objective optimization has been carried out. The energy loss (kWh) per year is calculated using the loading profile and loss modeling and it is used into the optimization algorithm.

F. Optimization Process

The multi-objective optimization has been performed, which minimize a vector of objectives $F(X)$ and returns the optimal parameters values of X.

$$\min F(X) \tag{34}$$

where

$$F(X) = [F_1(X), F_2(X)] \tag{35}$$

where $F_1(X)$ returns the energy loss (kWh). The total loss $(P_{fe} + P_{cu})$ are evaluated for each of the loading conditions and the total energy losses (kWh) are obtained as

$$F_1(X) = \frac{1}{1000} \sum_{i=1}^{j} (P_{fe_i} + P_{cu_i}) T_i \tag{36}$$

TABLE III
VALUES OF L_f AND C_f OF THE LCL FILTER

Parameters	Values
L_f	1200 μH (0.22 pu)
Shunt capacitance $C_f + C_d$	289 μF (0.15 pu)

where T_i is the time in hours during which the WECS output power is P_i and associated losses are $(P_{fe_i} + P_{cu_i})$.

$F_2(X)$ returns the volume of the active parts of the inductor (ltr.) and it is given as

$$F_2(X) = (V_{fe} + V_{cu}) * 1000 \tag{37}$$

where V_{fe} is the volume of the magnetic material and V_{cu} is the total volume of all the coils. The volume of the magnetic material is obtained as

$$V_{fe} = A_c\big(6W_l + 4W_w + 3(H_w - l_g)\big) \tag{38}$$

where A_c is the cross-sectional area of the core, W_l is the width of the limb, W_w is the width of the window, H_w is the height of the window, and l_g is the length of the air gap. The copper volume is given as

$$V_{cu} = 6N l_{mt} A_{cu} \tag{39}$$

where N is the number of turns, l_{mt} is the mean length of the turn, and A_{cu} is the cross-sectional area of the coil. The parameters that are optimized are

$$X = [N\ B_m\ J\ m\ W_c]^T \tag{40}$$

where B_m is the maximum flux density and J is the current density. W_c is the width of the coil (refer Fig. 3(c)). Once the system specifications and the constraints are defined, the optimization has been carried out. As the number of turns N and the number of layers m only take the integer values, mixed-integer optimization problem has been formulated. The steps followed for optimizing the system specified in Table I is shown in Fig. 9 and explained briefly hereafter.

1) Step 1: Value of the converter-side inductor L_f: The leakage inductance of the transformer is considered as a part of the grid-side inductor L_g and the use of any additional inductor is avoided. Therefore, the value of the L_g is fixed and the values of the L_f and C_f are obtained while observing the following constraints:

1) $I_h < I_h^*$ where h is the harmonic order $(2 \leq h \leq 180)$
2) Reactive power consumption in shunt branch $\leq 15\%$ of rated power.

The required value of the filter admittance is obtained using (18) and the values of the LCL harmonic filter is chosen to ensure that the admittance offered by the designed filter is lower than the required value of the filter admittance for all the individual harmonic components, as shown in Fig. 10. The calculated values of the L_f and C_f are listed in Table III.

2) Step 2: Derive dependent design variables: The dependent design variable are derived from the free design variables and the system specifications. The cross-sectional area of the core is obtained as

$$A_c = \frac{L_f I_{max}}{2N B_m} \tag{41}$$

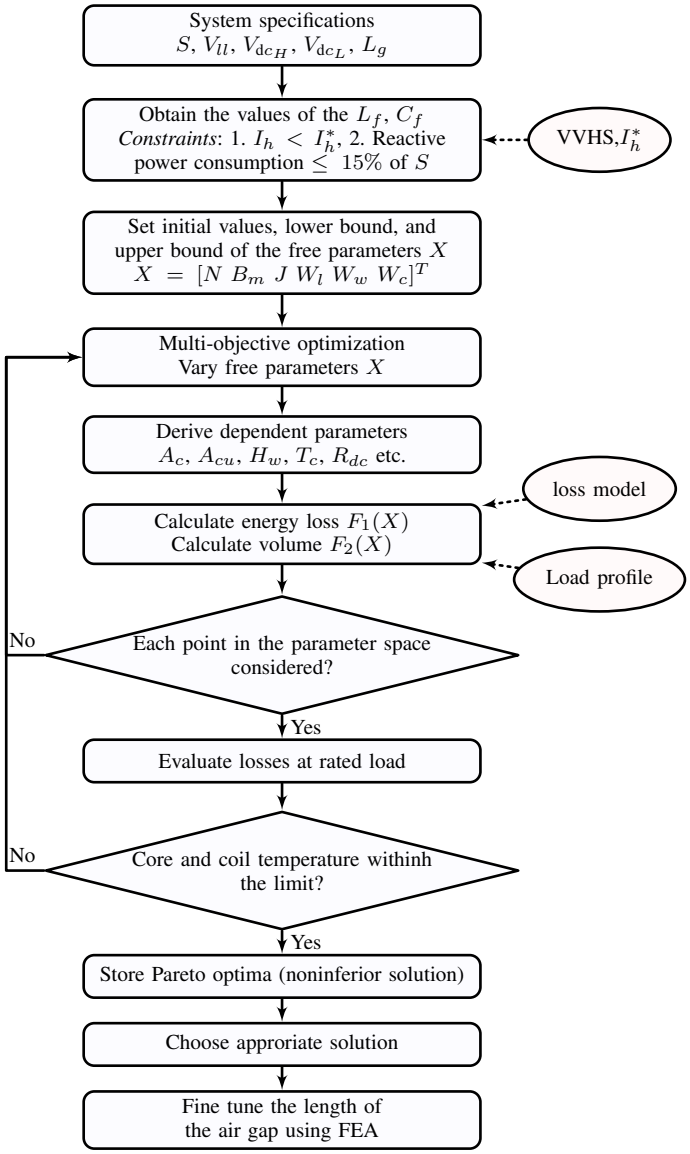

Fig. 9. Block diagram, which illustrates the steps of the optimization procedure.

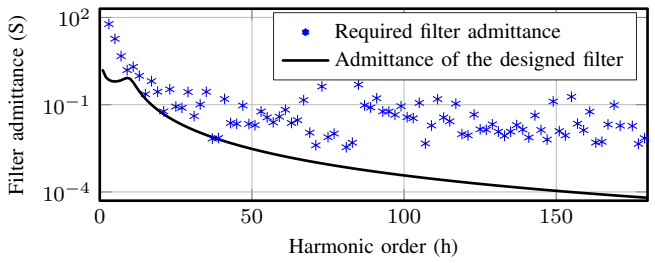

Fig. 10. Admittance variation of the designed filter along with the required value of the filter admittance.

where I_{max} is the rated current. The dimensions of the core is then obtained as $W_l D_l = A_c/k_s$, where k_s is the stacking factor. For simplicity, $W_l = B_l$ is assumed in this study. The cross-section area of the conductor is obtained as

$$A_{cu} = W_c T_c = \frac{I_{max}}{J} \tag{42}$$

TABLE IV
PARAMETER VALUES OF THE SELECTED DESIGN.

Item	Value	Item	Value	Item	Value
N	25	A_c	30200 mm^2	B_m	1.36 T
W_w	140 mm	J	4.08 A/mm^2	W_c	33 mm
A_{cu}	396 mm^2	H_w	980 mm	k_s	0.92
k_w	0.6	T_c	12 mm	m	2
k_i	0.96	α	1.55	β	1.87

3) Step 3: Objective function evaluation: The objective functions $F_1(x)$ and $F_2(x)$ are evaluated for the given set of parameters and specific mission profile. The core losses and the copper loss for each of the specific loading conditions, shown in Fig. 8, are evaluated. Using this information, the energy loss over one year period is evaluated. Similarly, the volume of both the core and the copper is also calculated.

4) Step 4: Air gap length: The liquid cooling effectively removes the heat generated due to the copper losses and allows designers to reduce the constant losses (mostly core losses) by increasing the number of turns N. This leads to an improvement in the energy efficiency. However, for a given value of the inductance, a larger number of turns also requires larger air gap, which leads to higher fringing flux. The solution is to use several small air gaps, which is achieved by using the discrete core blocks. The length of each of these air gaps and core blocks is limited to 2.5 mm and 30 mm, respectively. If any of these quantities is violated, the solution is discarded.

5) Step 5: Temperature estimation: The core and the copper losses are evaluated at the rated load conditions and the results are fed to the thermal network shown in Fig. 7(b). By solving the thermal network, temperature of the core (T_{fe}) and the coil (T_{cu}) is obtained. This gives the worst case temperature rise. If the temperature rise is above the prescribed value, the solution is discarded and the optimization steps are again executed for a new set of free variables.

6) Step 6: Pareto optima solutions: The energy loss and the volume of the inductor are closely coupled and competes with each other. For example, In a given system, the reduction in the volume often leads to the rise in the losses. As a result, there is no unique solution to the optimization problem and several noninferior solutions (Pareto front) are obtained. These solutions are stored. Depending upon the application, suitable design (out of these noninferior solutions) is chosen.

7) Step 7: FEA analysis: The length of the air gap during the optimization process is obtained using the simplified reluctance model. This may lead to the inductance value to deviate slightly from the desired value. Moreover, other non linearities are also neglected in the simplified model and it is very necessary to perform the Finite Element Analysis (FEA) to fine tune the length of the air gap so that the desired value of the inductance can be obtained. This has been achieved using by performing 'Optimetrics 'analysis in Ansys Maxwell.

V. Designed Parameters and Volumetric Comparison

A. Selected Design

A non-inferior (Pareto optimal) solution is obtained as shown in Fig. 11, where the reduction in the energy loss

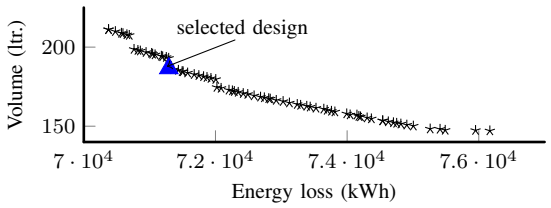

Fig. 11. Calculated volume and energy loss of the integrated inductor for different Pareto optimal solutions.

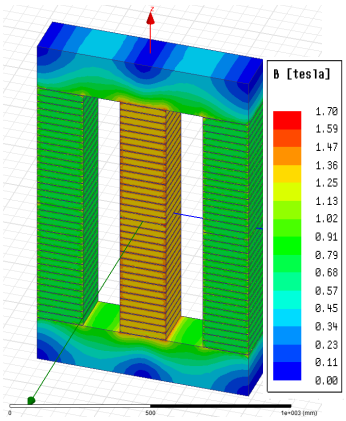

Fig. 12. Flux density distribution in the magnetic core. Both the coils on the central limb carry 1630 A current (peak of the rated current), whereas the other four coils on the side limbs carry half of peak value of the rated current in the opposite direction (-815 A).

requires increase in the volume. Out of these several possible design solutions, one that suits the application the most, has been selected, as shown in Fig. 11. The parameter values of the selected design are given in Table IV.

The volume of the inductor is 187.1 ltr. and the energy loss over one year span is 71291 kWh. The coils are designed to carry the rated current (1154 A) and can be wound using copper bars. The major harmonic component in the coil current is at 1.8 kHz and at this frequency, the increase in the ohmic losses in the ac resistance of the coil due to skin effect is insignificant. Therefore, the use of the copper bars for the coils is considered.

Multiple air gaps are achieved using the discrete core blocks and the length of each of the air gap is fine tuned using the FEA analysis. The FEA analysis is performed on the inductor geometry given in Table IV. The length of each of the air gap is fine tuned and it is found to be 2.46 mm. The flux density distribution in the inductor core is shown in Fig. 12. The inductance matrix is also obtained from the FEA and it is given in Table V. The line filter inductance is obtained from these value and it is given as

$$L_f = 1184\ \mu\text{H} \tag{43}$$

The core and the copper losses of the inductor over the whole operating range is shown in Fig. 13. The core losses and the copper losses at the full load conditions are 7.09 kW and 9.67 kW, respectively. The coolant flow in each of the duct is taken to be 0.06 l/s and the duct diameter D_d is 0.01 m. The inlet temperature of the coolant is assumed to be 20°C.

TABLE V
INDUCTANCES VALUES OBTAINED USING THE FINITE ELEMENT ANALYSIS. ALL VALUES ARE IN μH.

Coil	a_H	b_H	c_H	a_L	b_L	c_L
a_H	375	−84	−62	115	−19	−39
b_H	−84	384	−84	−19	104	−19
c_H	−62	−84	375	−39	−19	115
a_L	115	−19	−39	375	−84	−62
b_L	−19	104	−19	−84	384	−84
c_L	−39	−19	115	−62	−84	375

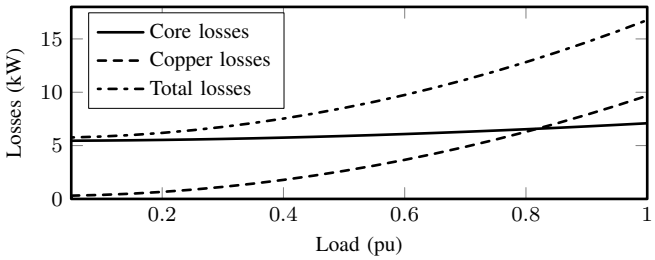

Fig. 13. Core and copper losses of the integrated inductor with different loading conditions.

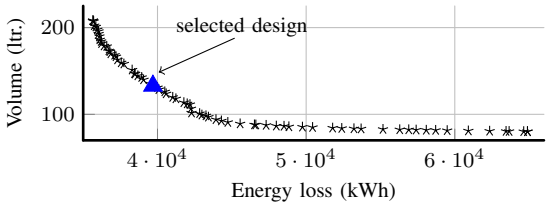

Fig. 14. Calculated volume and energy loss of the one of the separate inductors for different Pareto optimal solutions.

The core temperature at the rated load is calculated to be 74 °C, whereas the temperature of the coil is found to be 86 °C.

B. Volumetric comparison

The magnetic integration leads to a reduction in the size of the inductor. This has been demonstrated by comparing the volume of the integrated inductor with the volume of the inductors in a separate inductor case. The multi-objective optimization for the separate inductor case has been also carried out with an objective to minimize the energy loss and the volume. The mission profile and the solution space (range of the parameters that are optimized) are taken to be the same in both the cases. The converter-side inductance of both the HSC and the LSC are taken to be the same ($L_{f_H} = L_{f_L} = 600$ μH). The value of each of the converter-side inductor is taken to be 600 μH to ensure same attenuation of the harmonic frequency components in both the separate inductor case and the integrated inductor case.

The non-inferior (Pareto optimal) solutions for the separate inductor are shown in Fig. 14. Out of many possible solutions, one design is selected with the volume of 132.8 ltr. and the energy loss of 39693 kWh. The comparison of the various performance parameters of both the separate inductor case and the integrated inductor case is given in Table VI.

The volume of the magnetic material of the integrated

TABLE VI
VOLUME AND ENERGY LOSS COMPARISON.

Parameter	Separate inductor ($L_{f_H} + L_{f_L}$)	Integrated inductor	Reduction (%)
Volume of active materials (ltr.)	$2 \times 132.8 = 265.6$	187.1	29.5 %
Volume of magnetic materials (ltr.)	$2 \times 88.65 = 177.3$	132.2	25.4 %
Volume of copper (ltr.)	$2 \times 44.15 = 88.3$	54.9	37.8 %
Energy loss (kWh)	$2 \times 39693 = 79386$	71291	10.1 %
Total losses at full load (kW)	$2 \times 8.38 = 16.76$	14.86	11.3 %

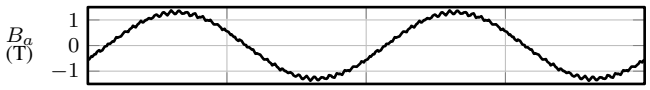

Fig. 15. Simulated flux density waveform in the limb of phase a.

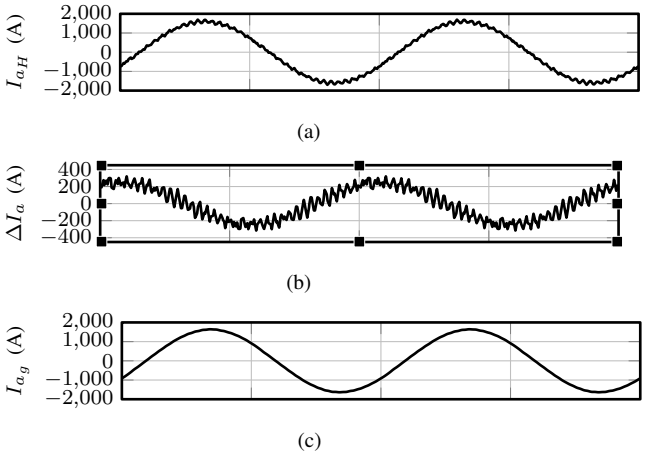

Fig. 16. Simulation results. (a) Flux density waveform in the limb of phase a, (b) Output current of the high-side converter I_h, (c) Current through the shunt branch of the LCL filter, (d) Current through the open-end transformer windings.

inductor is calculated to be 132.2 ltr, compared to the 177.3 ltr. for the separate inductors. This demonstrates around 41.1 ltr (25.4%) reduction in the magnetic material. Assuming the use of the 0.35 mm grain oriented steel, which has a density of 7.63 kg/ltr, 41.1 ltr reduction in the volume would translates to 314 kg reduction in the weight of the magnetic material. In addition, 37.8% reduction in the copper volume is also achieved. The energy loss in the integrated inductor for the given mission profile is 71291 kWh against 79386 kWh for the separate inductor case.

VI. SIMULATION AND HARDWARE RESULTS

The time domain simulations have been carried out using PLECS. The parameters used in the simulations are specified in Table I. The integrated inductor is modeled using the magnetic toolbox, which uses the permanence model.

The converter was simulated at the rated power and the simulated flux density waveform in one of the limb is shown in Fig. 15. The flux density has a dominant fundamental frequency component with major harmonic component at the 2nd carrier harmonic frequency. The output current of the HSC is shown in Fig. 16(a), which has a major harmonic component at 2nd carrier frequency harmonic. As the leg current in the

TABLE VII
VALUES OF L_f AND C_f OF THE LCL FILTER

Parameters	Values
L_f	9 mH (0.195 pu)
Shunt capacitance C_f	14 μF (0.065 pu)
Damping capacitance C_d	10 μF (0.045 pu)
Damping resistor R_d	30 Ω

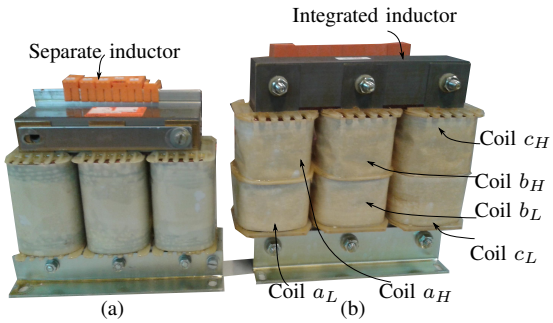

Fig. 17. Photos of the converter-side inductor of the LCL harmonic filter. (a) 4.6 mH inductor used in the separate inductor case, where two such inductors are required. (b) 9 mH integrated inductor which magnetically integrates two separate inductors.

HSC and the LSC is the same ($I_{a_H} = I_{a_L}$), only the current of the HSC I_{a_H} is shown. The shunt branch of the LCL filter offers low impedance path to the harmonic components, as shown in Fig. 16(b). As a result, the injected grid currents have the desired waveform quality, as shown in Fig. 16(c).

A small scale prototype has been built to verify the effectiveness of the proposed inductor. The specifications of the small scale system is given in Table I. The dc-link voltages for the HSC and the LSC were derived from two separate dc power supplies. The converter system was connected to the ac power source from the California Instruments (MX-35), which was used to emulate harmonic free grid. The filter arrangement is shown in Fig. 1, where the LCL filter, along with the R_d/C_d damping branch is used. The values of the filter parameters are given in Table VII. A 11 kVA, 230/400 V three-phase transformer is employed where the 230 V star-connected windings are reconfigured to obtain the open-end transformer windings.

The integrated inductor is realized using the standard laminated steel (0.35 mm) and the coils are wound using the AWG 11. Each coils have 102 turns and the length of the air gap is 2.014 mm. The photo of the inductor prototype is shown in Fig. 17.

The voltages across the capacitive branch of the LCL filter $V_{x_H x_L}$ and the output currents of the HSC I_{x_H} are sensed and used as a feedback variables to implement the closed-loop control system. The control is implemented using

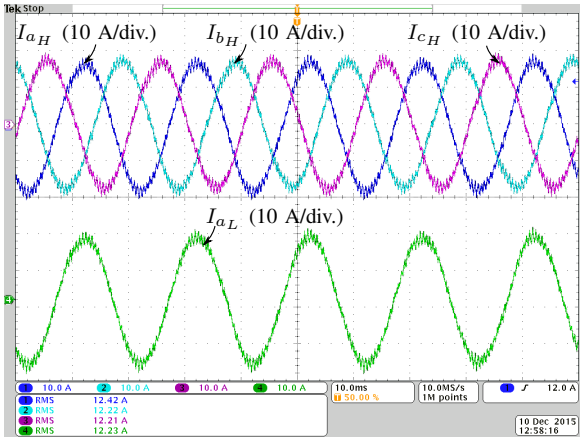

(a)

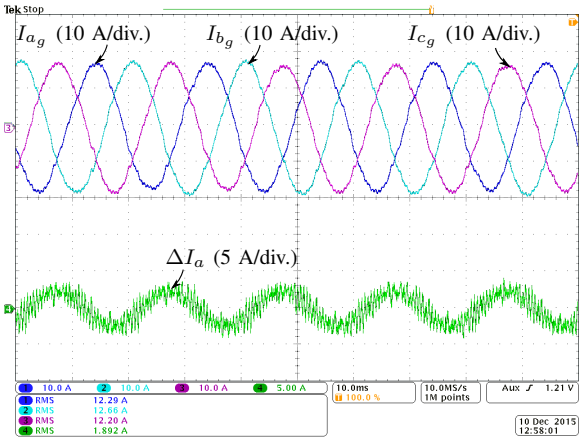

(b)

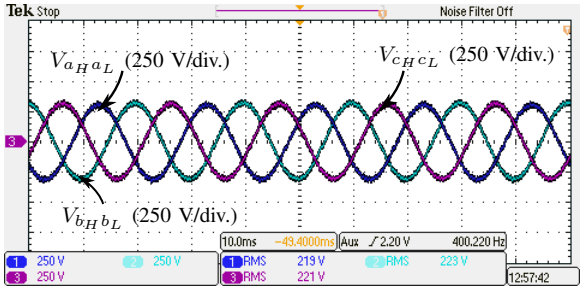

(c)

Fig. 18. Experimental waveforms with the rated active current injected to the grid. (a) Ch1: I_{a_H}, Ch2: I_{b_H}, Ch3: I_{c_H}, and Ch4: I_{a_L}, (b) Ch1: I_{a_g}, Ch2: I_{b_g}, Ch3: I_{c_g}, and Ch4: ΔI_a, (c) Ch1: $V_{a_H a_L}$, Ch2: $V_{b_H b_L}$, and Ch3: $V_{c_H c_L}$.

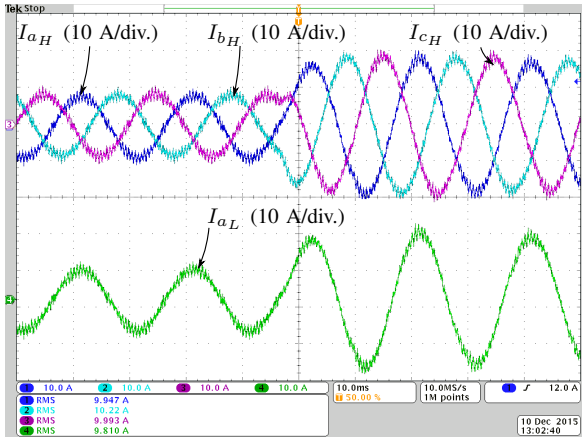

(a)

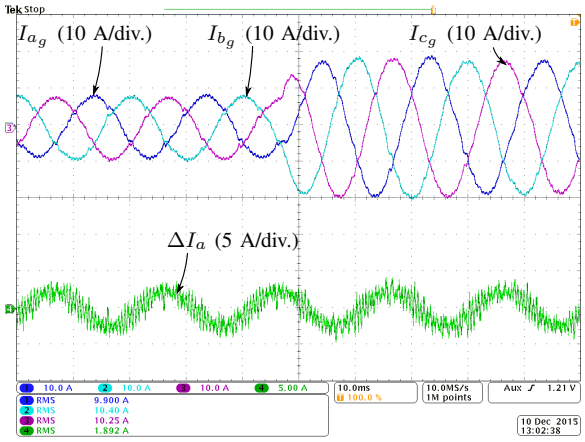

(b)

Fig. 19. Experimental waveforms for a step response when the reference current was changed from 0.5 pu to 1 pu. (a) Ch1: I_{a_H}, Ch2: I_{b_H}, Ch3: I_{c_H}, and Ch4: I_{a_L}, (b) Ch1: I_{a_g}, Ch2: I_{b_g}, Ch3: I_{c_g}, and Ch4: ΔI_a.

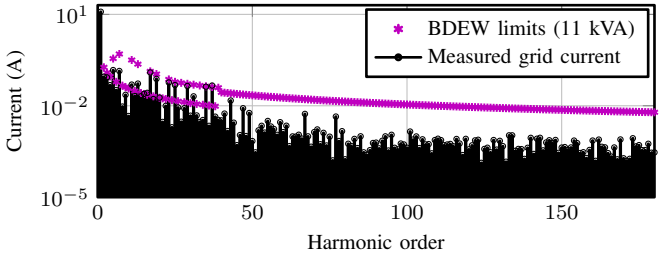

Fig. 20. Harmonic spectra of the measured grid current and associated BDEW harmonic injection limits.

TMS320F28346 floating-point digital signal processor. The converters are controlled to inject the rated current to the grid and the experimental waveforms during the steady-state condition are shown in Fig. 18. The output current of LSC of phase a is also shown in Fig. 18(a). The converter-side currents have a major harmonic components, concentrated around the second carrier harmonic frequency. The transient performance has been verified by applying the step change in the reference current from 0.5 pu to 1 pu and the corresponding current waveforms are shown in Fig. 19. The harmonic spectra of the injected current is shown in Fig. 20, where it is evident that the magnitude of the individual harmonic components of the injected current is within the specified BDEW limits.

The power losses of the integrated inductor at different loading conditions have been measured using the Voltech PM3000 power analyzer. The measured losses are shown in Table VIII. The losses of the integrated inductor at the full load condition is around 1% of the rated power.

The magnetic integration of the converter-side inductor of the HSC and the LSC leads to the substantial reduction in the volume and the energy loss without compromising the harmonic performance. This has been verified by comparing the harmonic spectra of the line current in the case of the

TABLE VIII
MEASURED LOSSES IN THE INTEGRATED INDUCTOR.

Load	0.25 pu	0.5 pu	0.75 pu	1 pu
Losses (W)	42	55	79	109

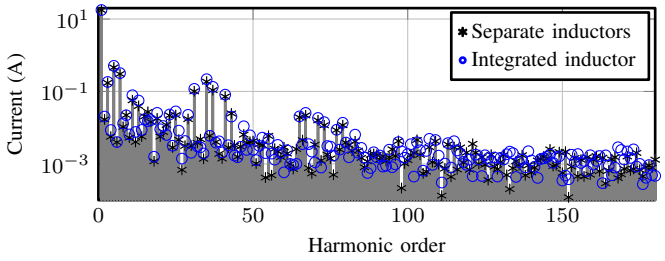

Fig. 21. Harmonic spectra of the measured grid current.

LCL filter integrated inductor with that of the LCL filter with separate inductors. Off the shelf 4.6 mH, 16A three-phase three-limb inductors are used in the separate inductor case ($L_{f_H} = L_{f_L} = 4.6$ mH) and the results are compared with the designed integrated inductor with $L_f = 9$ mH. The harmonic spectra of the line current in both the cases are shown in Fig. 21, which demonstrates that the harmonic performance is not compromised by the magnetic integration. The magnitude of the harmonic components are slightly smaller in the case of the separate inductor, as the effective value of L_f is 9.2 mH, as against the 9 mH in the case of the integrated inductor.

VII. CONCLUSION

An integrated inductor for the the dual-converter fed open-end transformer topology is proposed. The dual-converter system often comprises of two identical VSCs. These two VSCs use two separate converter-side inductors for the LCL filter implementation. For the dual-converter system, the output currents of the given phase of both VSCs are equal. This property of the dual-converter system is exploited to cancel out the flux in one of the yokes of both the inductors through the magnetic integration. Moreover, a multi-objective optimization has been performed to identify best possible solutions which leads to the minimization of the energy loss and minimization of the volume of the inductor. The size reduction achieved through magnetic integration is demonstrated by comparing the volume of the proposed solution with the separate inductor case. The integrated inductor leads to 25.4% reduction in the volume of the magnetic material. This translates to 314 kg reduction in the weight of the magnetic component for the 6.6 MVA, 3.3 kV WECS system. The performance of the filter has been verified by simulation and experimental studies.

ACKNOWLEDGMENTS

The authors would like to thank the Innovation Foundation through the Intelligent Efficient Power Electronics (IEPE) technology platform for supporting the related research.

REFERENCES

[1] G. Grandi, C. Rossi, D. Ostojic, and D. Casadei, "A new multilevel conversion structure for grid-connected pv applications," *IEEE Trans. Ind. Electron.*, vol. 56, no. 11, pp. 4416–4426, Nov 2009.

[2] H. Stemmler and P. Guggenbach, "Configurations of high-power voltage source inverter drives," in *Proc. of Fifth European Conference on Power Electronics and Applications*, Sep 1993, pp. 7–14 vol.5.

[3] T. Boller, J. Holtz, and A. Rathore, "Optimal pulsewidth modulation of a dual three-level inverter system operated from a single DC link," *IEEE Trans. Ind. Appl.*, vol. 48, no. 5, pp. 1610–1615, Sept 2012.

[4] N. Bodo, M. Jones, and E. Levi, "A space vector pwm with common-mode voltage elimination for open-end winding five-phase drives with a single DC supply," *IEEE Trans. Ind. Electron.*, vol. 61, no. 5, pp. 2197–2207, May 2014.

[5] M. R. Baiju, K. Mohapatra, R. S. Kanchan, and K. Gopakumar, "A dual two-level inverter scheme with common mode voltage elimination for an induction motor drive," *IEEE Trans. Power Electron.*, vol. 19, no. 3, pp. 794–805, May 2004.

[6] E. Levi, "Multiphase electric machines for variable-speed applications," *IEEE Trans. Ind. Appl.*, vol. 55, no. 5, pp. 1893–1909, May 2008.

[7] F. Blaabjerg, M. Liserre, and K. Ma, "Power electronics converters for wind turbine systems," *IEEE Trans. Ind. Appl.*, vol. 48, no. 2, pp. 708–719, March 2012.

[8] R. P. Wojda and M. K. Kazimierczuk, "Analytical optimization of solid -round-wire windings," *IEEE Trans. Ind. Electron.*, vol. 60, no. 3, pp. 1033–1041, March 2013.

[9] R. P. Wojda and M. K. Kazimierczuk, "Magnetic field distribution and analytical optimization of foil windings conducting sinusoidal current," *IEEE Magn. Letters*, vol. 4, pp. 0 500 204–0 500 204, 2013.

[10] M. K. Kazimierczuk, *High-Frequency Magnetic Components (2nd Edition)*. John Wiley and Sons, 2013.

[11] J. R. R. Zientarski, R. C. Beltrame, D. B. Candido, M. l. D. S. Martins, and H. L. Hey, "Design methodology for universal line input boost power factor correction magnetics," *IET Power Electronics*, vol. 4, no. 6, pp. 715–724, July 2011.

[12] D. O. Boillat, F. Krismer, and J. W. Kolar, "Design space analysis and $\rho - \eta$ pareto optimization of lc output filters for switch-mode ac power sources," *IEEE Trans. Power Electron.*, vol. 30, no. 12, pp. 6906–6923, Dec 2015.

[13] G. Gohil, L. Bede, R. Teodorescu, T. Kerekes, and F. Blaabjerg, "Integrated inductor for interleaved operation of two parallel three-phase voltage source converters," in *Proc. 17th European Conference on Power Electronics and Applications (EPE'15 ECCE-Europe)*, Sept 2015, pp. 1–10.

[14] G. Gohil, L. Bede, R. Teodorescu, T. Kerekes, and F. Blaabjerg, "An integrated inductor for parallel interleaved three-phase voltage source converters," *IEEE Trans. Power Electron.*, vol. 31, no. 5, pp. 3400–3414, May 2016.

[15] G. Gohil, L. Bede, R. Teodorescu, T. Kerekes, and F. Blaabjerg, "An integrated inductor for parallel interleaved vscs and pwm schemes for flux minimization," *IEEE Trans. Ind. Electron.*, vol. 62, no. 12, pp. 7534–7546, Dec 2015.

[16] G. Gohil, L. Bede, R. Teodorescu, T. Kerekes, and F. Blaabjerg, "An integrated inductor for parallel interleaved vscs connected in a whiffletree configuration," *in Proc. IEEE Energy Conversion Congress and Exposition*, pp. 5952–5959, Sept 2015.

[17] G. Gohil, L. Bede, R. Teodorescu, T. Kerekes, and F. Blaabjerg, "Magnetic integration for parallel interleaved vscs connected in a whiffletree configuration," *IEEE Trans. Power Electron.*, [Online early access], DOI: 10.1109/TPEL.2015.2514182, 2016.

[18] S. Cuk, "A new zero-ripple switching dc-to-dc converter and integrated magnetics," in *Proc. IEEE Power Electronics Specialists Conference*, June 1980, pp. 12–32.

[19] D. Pan, X. Ruan, C. Bao, W. Li, and X. Wang, "Magnetic integration of the lcl filter in grid-connected inverters," *IEEE Trans. Power Electron.*, vol. 29, no. 4, pp. 1573–1578, April 2014.

[20] V. Valdivia, J. Pleite, P. Zumel, C. Gonzalez, and A. Roldan, "Three phase lcl filter and transformer with integrated magnetics for grid connected converters," in *Proc. 34th Annual Conference of IEEE Industrial Electronics*, Nov 2008, pp. 1027–1032.

[21] C. W. T. McLyman, *Transformer and Inductor Design Handbook*. Boca Raton, FL: CRC Press, 2003.

[22] D. G. Holmes and T. A. Lipo, *Pulse Width Modulation for Power Converters: Principles and Practice*. Hoboken, NJ: Wiley-IEEE Press, 2003.

[23] A. Rockhill, M. Liserre, R. Teodorescu, and P. Rodriguez, "Grid-filter design for a multimegawatt medium-voltage voltage-source inverter," *IEEE Trans. Ind. Electron.*, vol. 58, no. 4, pp. 1205–1217, 2011.

[24] "Technical guidline: Generating plants connected to the medium-voltage network." BDEW Bundesverband der Energie- und Wasserwirtschaft e.V., [Online]. Available: http://www.bdew.de, 2008.

[25] S. Araujo, A. Engler, B. Sahan, and F. Antunes, "LCL filter design for grid-connected NPC inverters in offshore wind turbines," in *Proc. Power Electronics, 2007. ICPE '07. 7th Internatonal Conference on*, 2007, pp. 1133–1138.
[26] G. Gohil, L. Bede, R. Teodorescu, T. Kerekes, and F. Blaabjerg, "Line filter design of parallel interleaved vscs for high-power wind energy conversion systems," *IEEE Trans. Power Electron.*, vol. 30, no. 12, pp. 6775–6790, Dec 2015.
[27] G. Gohil, L. Bede, R. Teodorescu, T. Kerekes, and F. Blaabjerg, "Design of the trap filter for the high power converters with parallel interleaved VSCs," in *Proc. 40th Annual Conference on IEEE Industrial Electronics Society, IECON 2014*, Oct 2014, pp. 2030–2036.
[28] K. Venkatachalam, C. Sullivan, T. Abdallah, and H. Tacca, "Accurate prediction of ferrite core loss with nonsinusoidal waveforms using only steinmetz parameters," in *Computers in Power Electronics, 2002. Proceedings. 2002 IEEE Workshop on*, 2002, pp. 36–41.
[29] J. Li, T. Abdallah, and C. Sullivan, "Improved calculation of core loss with nonsinusoidal waveforms," in *Industry Applications Conference, 2001. Thirty-Sixth IAS Annual Meeting. Conference Record of the 2001 IEEE*, vol. 4, 2001, pp. 2203–2210 vol.4.
[30] A. Hava, R. Kerkman, and T. Lipo, "Simple analytical and graphical methods for carrier-based PWM-vsi drives," *IEEE Trans. Power Electron.*, vol. 14, no. 1, pp. 49–61, Jan 1999.
[31] G. Narayanan and V. T. Ranganathan, "Analytical evaluation of harmonic distortion in PWM AC drives using the notion of stator flux ripple," *IEEE Trans. Power Electron.*, vol. 20, no. 2, pp. 466–474, 2005.
[32] P. Dowell, "Effects of eddy currents in transformer windings," *Proceedings of the Institution of Electrical Engineers,*, vol. 113, no. 8, pp. 1387–1394, August 1966.
[33] W. Hurley, E. Gath, and J. Breslin, "Optimizing the ac resistance of multilayer transformer windings with arbitrary current waveforms," *IEEE Trans. Power Electron.*, vol. 15, no. 2, pp. 369–376, Mar 2000.
[34] A. V. d. Bossche and V. C. Valchev, *Inductors and Transformers for Power Electronics*. Boca Raton, FL: CRC Press, 2004.

Ghanshyamsinh Gohil (S'13) received the M.Tech. degree in electrical engineering with specialization in power electronics and power systems from the Indian Institute of Technology-Bombay, Mumbai, India, in 2011. In March 2016, he obtained the PhD degree from the Department of Energy Technology, Aalborg University, Denmark.

Prior to joining PhD, he was with Siemens Corporate Technology where he worked on the Micro-Grid project. He also worked on the PV systems and the power quality issues during his employment at Crompton Greaves Global R&D center. He is currently working as a Post-Doctoral Researcher with the Department of Energy Technology, Aalborg University, Denmark. His research interests include wide band-gap devices, smart energy systems, parallel operation of voltage source converters, pulsewidth modulation techniques and the design of the inductive power components.

Lorand Bede (S'13) received the engineering degree in electrical engineering from Sapientia Hungarian University of Transylvania, Targu Mures, Romania in 2011, with specialization is Automation and Industrial Informatics, the MSc. degree in Power Electronics and Drives from Aalborg University, Aalborg, Denmark, in 2013. For 6 months he was a visiting PhD student at the School of Electrical Engineering in 2015. Currently he is working towards his PhD degree at the Department of Energy Technology, at Aalborg University, Aalborg. His research interest include grid connected applications based on parallel interleaved converters for renewable applications.

Remus Teodorescu (S'94-A'97-M'99-SM'02-F'12) received the Dipl.Ing. degree in electrical engineering from Polytechnical University of Bucharest, Romania in 1989, and PhD. degree in power electronics from University of Galati, Romania, in 1994. In 1998, he joined Aalborg University, Department of Energy Technology, power electronics section where he currently works as full professor. Since 2013 he is a visiting professor at Chalmers University. He has coauthored the book Grid Converters for Photovoltaic and Wind Power Systems, ISBN: 978-0-470-05751-3, Wiley 2011 and over 200 IEEE journals and conference papers. His areas of interests includes: design and control of grid-connected converters for photovoltaic and wind power systems, HVDC/FACTS based on MMC, SiC-based converters, storage systems for utility based on Li-Ion battery technology. He was the coordinator of the Vestas Power Program 2008 to 2013.

Tamas Kerekes (S'06-M'09) obtained his Electrical Engineer diploma in 2002 from Technical University of Cluj, Romania, with specialization in Electric Drives and Robots. In 2005, he graduated the Master of Science program at Aalborg University, Institute of Energy Technology in the field of Power Electronics and Drives. In Sep. 2009 he obtained the PhD degree from the Institute of Energy Technology, Aalborg University. The topic of the PhD program was: "Analysis and modeling of transformerless PV inverter systems". He is currently employed as an Associate professor and is doing research at the same institute within the field of grid connected renewable applications. His research interest include grid connected applications based on DC-DC, DC-AC single- and three-phase converter topologies focusing also on switching and conduction loss modeling and minimization in case of Si and new wide-bandgap devices.

Frede Blaabjerg (S'86-M'88-SM'97-F'03) was with ABB-Scandia, Randers, Denmark, from 1987 to 1988. From 1988 to 1992, he was a Ph.D. Student with Aalborg University, Aalborg, Denmark. He became an Assistant Professor in 1992, an Associate Professor in 1996, and a Full Professor of power electronics and drives in 1998. His current research interests include power electronics and its applications such as in wind turbines, PV systems, reliability, harmonics and adjustable speed drives. He has received 17 IEEE Prize Paper Awards, the IEEE PELS Distinguished Service Award in 2009, the EPE-PEMC Council Award in 2010, the IEEE William E. Newell Power Electronics Award 2014 and the Villum Kann Rasmussen Research Award 2014. He was an Editor-in-Chief of the IEEE TRANSACTIONS ON POWER ELECTRONICS from 2006 to 2012. He has been Distinguished Lecturer for the IEEE Power Electronics Society from 2005 to 2007 and for the IEEE Industry Applications Society from 2010 to 2011. He is nominated in 2014 and 2015 by Thomson Reuters to be between the most 250 cited researchers in Engineering in the world.